Acta Pharmaceutica Sinica B 2022;12(6):2934–2949

Chinese Pharmaceutical Association
Institute of Materia Medica, Chinese Academy of Medical Sciences

Acta Pharmaceutica Sinica B

www.elsevier.com/locate/apsb
www.sciencedirect.com

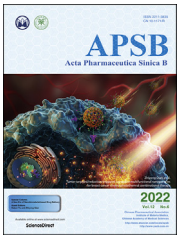

ORIGINAL ARTICLE

Nanoparticles with rough surface improve the therapeutic effect of photothermal immunotherapy against melanoma

Jiao Xue, Yining Zhu, Shuting Bai, Chunting He, Guangsheng Du, Yuandong Zhang, Yao Zhong, Wenfei Chen, Hairui Wang, Xun Sun*

Key Laboratory of Drug-Targeting and Drug Delivery System of the Education Ministry and Sichuan Province, Sichuan Engineering Laboratory for Plant-Sourced Drug and Sichuan Research Center for Drug Precision Industrial Technology, West China School of Pharmacy, Sichuan University, Chengdu 610041, China

Received 15 October 2021; received in revised form 9 November 2021; accepted 20 November 2021

KEY WORDS

Photothermal therapy;
Immunotherapy;
Rough surface;
Polydopamine-coated silica nanoparticles;
JQ-1;
Melanoma

Abstract Photothermal therapy has been intensively investigated for treating cancer in recent years. However, the long-term therapeutic outcome remains unsatisfying due to the frequently occurred metastasis and recurrence. To address this challenge, immunotherapy has been combined with photothermal therapy to activate anti-tumor immunity and relieve the immunosuppressive microenvironment within tumor sites. Here, we engineered silica-based core–shell nanoparticles (JQ-1@PSNs-R), in which silica cores were coated with the photothermal agent polydopamine, and a bromodomain-containing protein 4 (BRD4) inhibitor JQ-1 was loaded in the polydopamine layer to combine photothermal and immune therapy for tumor elimination. Importantly, to improve the therapeutic effect, we increased the surface roughness of the nanoparticles by hydrofluoric acid (HF) etching during the fabrication process, and found that the internalization of JQ-1@PSNs-R was significantly improved, leading to a strengthened photothermal killing effect as well as the increased intracellular delivery of JQ-1. In the animal studies, the multifunctional nanoparticles with rough surfaces effectively eradicated melanoma *via* photothermal therapy, successfully activated tumor-specific immune responses against residual tumor cells, and further prevented tumor metastasis and recurrence. Our results indicated that JQ-1@PSNs-R could serve as an innovative and effective strategy for combined cancer therapy.

*Corresponding author. Tel./fax: +86 28 85502307.
E-mail address: sunxun@scu.edu.cn (Xun Sun).

Peer review under responsibility of Chinese Pharmaceutical Association and Institute of Materia Medica, Chinese Academy of Medical Sciences

https://doi.org/10.1016/j.apsb.2021.11.020

1. Introduction

Cancer is currently one of the leading causes of death all over the world, and conventional treatments including surgery, chemotherapy and radiation therapy remain unsatisfactory due to hypoimmunity and systemic toxicity[1]. In recent years, photothermal therapy has aroused attention because of its minimal invasion and superior cancer-killing capability[2]. Photosensitizers such as indocyanine green (ICG), IR780 and chlorin e6 (Ce6) are delivered to tumors and then irradiated with a laser, generating cancer-killing heat to eliminate the tumor[3]. While photothermal therapy can effectively eradicate many tumor cells, the risk of tumor recurrence is still high when resident tumor cells evade host immune responses[4]. Consequently, the emerging photo-mediated immunotherapy which combines the tumor-destroying capability of photothermal therapy with the immune-activating effect of immunotherapy becomes a more rational strategy[5–9].

Recently, polydopamine-based nanoparticles have been increasingly investigated. Polydopamine-mediated photothermal therapy has unique advantages to be combined with immune therapy including (1) the preparation of polydopamine is carried out in an alkaline solution at room temperature *via* self-polymerization and oxidation, during which other therapeutics such as low-molecular-weight drug can be easily encapsulated[10–12]; (2) the outstanding biodegradable and biocompatible properties of polydopamine provide sustained drug release and highly clinical translation capability[13]; (3) the polydopamine contains catechol groups which mediate the adhesion to other substances, making antigen adsorption possible[14]. The photothermal effect of polydopamine would kill major tumor tissues directly, and then the tumor antigens released from the lysed tumor cells after the photothermal therapy would adhere to the surface of polydopamine-based nanoparticles, which is beneficial to increase their uptake by dendritic cells and trigger the subsequent immune responses[15].

Additionally, the physical properties of nanoparticles could have a significant influence on the therapeutic effect of drugs. Previous reports have shown that by optimizing nanoparticle parameters including size[16,17], shape[17–20], surface charge[21,22], hydrophobicity[23,24] and stiffness[25,26], the therapeutical potency of the nanoparticles could be robustly improved. As another important physical parameter of nanoparticles, the surface roughness could also significantly affect the cell entry and intracellular behaviors of the nanoparticles[27], which will ultimately influence the therapeutic efficacy of formulations. However, very few studies have explored this relationship due to the difficulties of preparing nanoparticles with different roughness on the same material. Herein, we chose the silica nanoparticles, one of the widely used vehicles for delivering drugs and antigens into cells due to their biocompatibility, easy functionalization and certain adjuvant properties, as the supportive frameworks to study the effect of nanoparticle surface roughness on tumor treatment.

Immune checkpoint blockade therapy has been one of the most promising treatments in clinical use since the discovery of protein receptors that function as the immune checkpoint and downregulate immune responses such as cytotoxic T-lymphocyte-associated protein 4 (CTLA-4) and programmed cell death-1 (PD-1)[28,29]. The receptor-specific antibodies (*e.g.*, atezolizumab, avelumab and ipilimumab) have been widely used in clinics for reactivating antitumor immunity[30]. However, these receptor-specific antibodies have many defects, such as high price, instability and requiring frequent injections[31]. Therefore, PD-1/PD-L1 inhibitors with low molecular weight become hot candidates for cancer immunotherapy[32]. JQ-1 is a newly discovered highly specific inhibitor for the extra-terminal motif family of bromodomains (BET)[33–36]. After being internalized by cells, JQ-1 can reduce the expression of PD-L1 on cancer cells, dendritic cells as well as tumor-associated macrophages[37]. Compared with monoclonal antibodies of immune checkpoint inhibitors, JQ-1 is much more stable, but multiple injections are still needed to achieve a satisfactory anti-tumor effect[38]. To reduce the injection frequency and improve patient compliance[39], a new sustained-release delivery system for JQ-1 is in need[40], As polydopamine has the property of being slowly degraded under physiological conditions[41], the JQ-1-loaded polydopamine nanoparticles are expected to show a sustained release pattern.

Herein, we engineered novel core–shell nanoparticles (JQ-1@PSNs-R) with rough surfaces to achieve a synergistic anticancer effect. To prepare nanoparticles with different surface roughness, we choose organic-inorganic hybrid silica nanoparticles. After simply etching by hydrofluoric acid (HF), the organic part of nanoparticles was eroded and the silica nanoparticles with rough surfaces were obtained[42]. Then, the rough and smooth silica nanoparticles were both coated with polydopamine and the polydopamine-coated nanoparticles with different surface roughness were finally obtained and studied in follow-up research. In our nanoparticles (JQ-1@PSNs-R), polydopamine loaded with JQ-1 served as shells and the silica nanoparticles served as cores. After laser irradiation, polydopamine generated cancer-killing heat to eliminate most tumor cells. The increased roughness of nanoparticles markedly elevated cellular uptake, allowing the loaded JQ-1 effectively to enter the residual tumor cells. Then the released JQ-1 further inhibited the PD-L1 expression to help T cells eliminate the residual cancer cells[43]. Overall, JQ-1@PSNs-R effectively eradicated melanoma under laser irradiation, and the codelivery of JQ-1 which reduced the expression of PD-L1 on cancer cells simultaneously activated the immune system and reduced the risk of tumor recurrence and metastasis (Scheme 1).

2. Materials and methods

2.1. Materials

Tetraethylorthosilane (TEOS), ethanol, $NH_3 \cdot H_2O$ and hydrofluoric acid (HF) were purchased from Chengdu Chron Chemicals Co., Ltd. (Chengdu, China). *N*-[3-(Trimethoxysilyl)propyl]ethylenediamine (TSD) was purchased from Huaxia Reagent (Chengdu, China). Dopamine hydrochloride and Tris base were purchased from Aladdin (Shanghai, China) and BioFroxx (Einhausen, Germany), respectively. JQ-1 was obtained from CNS Pharmaceuticals (Houston, TX, USA). Fluorescein diacetate and propidium iodide were obtained from Solarbio (Beijing, China). The CytoTox 96® Non-Radioactive Cytotoxicity Assay Kit and the Cell Counting Kit-8 (CCK-8) were purchased from Promega (Madison, WI, USA) and Dojindo (Kumamoto, Japan), respectively. ELISA Kits for mouse IL-6, TNF-α and IFN-γ were purchased from Thermo Fisher Scientific (Waltham, MA, USA). Pierce BCA Kit and SDS-PAGE Kit were bought from Thermo Fisher Scientific and Beyotime (Shanghai, China). All flow cytometry antibodies used in the experiment were purchased from Biolegend (San Diego, CA, USA).

2.2. Cell lines and animals

Murine melanoma cell line B16F10 was purchased from the American Type Culture Collection (Rockville, MD, USA). Dendritic cell line DC 2.4 was kindly provided by the Third Military Medical University. Healthy male C57BL/6 mice were purchased

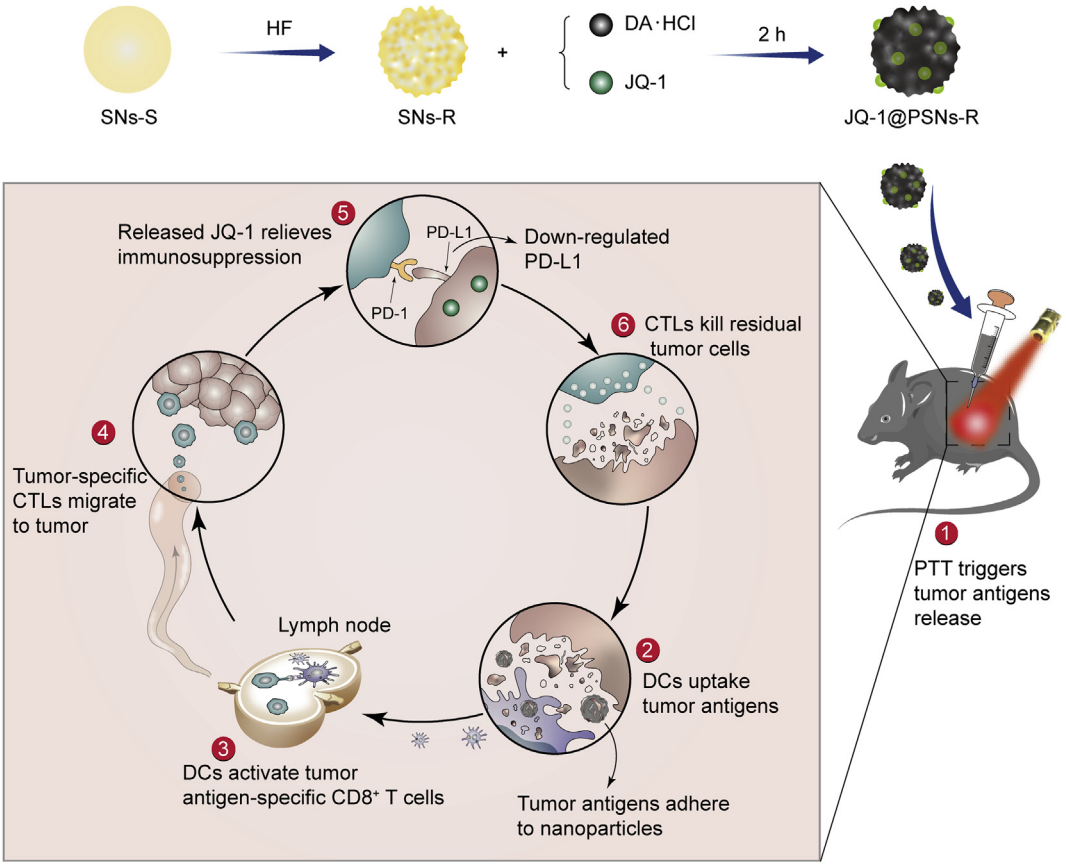

Scheme 1 Schematic illustration of JQ-1@PSNs-R-based photothermal immunotherapy. The smooth silica nanoparticles (SNs-S) were etched by hydrofluoric acid (HF) to obtain rough silica nanoparticles (SNs-R). By oxidative self-polymerization of dopamine hydrochloride (DA·HCl), JQ-1 encapsulated polydopamine layer was coated on SNs-R, and the JQ-1@PSNs-R were obtained. After intratumoral injection of JQ-1@PSNs-R and laser irradiation, the photothermal therapy (PTT) kills most tumor cells and triggers the release of tumor antigens. Due to the adhesive properties of polydopamine, the released tumor antigens adhere to the surface of nanoparticles, which promotes the uptake of antigens by dendritic cells (DCs). The DCs migrate to nearby lymph nodes and activate cytotoxic lymphocytes (CTLs). Meanwhile, the JQ-1@PSNs-R effectively downregulate the PD-L1 expression and relieve immunosuppression at the tumor site. Finally, the activated CTLs migrate to tumor sites and eliminate residual tumor cells.

from Hunan Slac Jingda Laboratory Animal Co., Ltd. (Changsha, China). All experimental procedures were executed according to the protocols approved by the Institutional Animal Care and Ethics Committee of Sichuan University.

2.3. *Synthesis and characterization of nanoparticles*

Under stirring condition, 4 mL ethanol solution of TSD (12 μL/mL) and 4 mL TEOS were added to 30 mL ethanol solution of ammonia (0.1 mL/mL) at the speed of 1 mL/min. Then 7 mL ethanol solution of TEOS (0.05 mL/mL) was added to the system dropwise. The system was kept stirring for 2 h. After reaction, we obtained smooth Si NPs (SNs-S) by washing and centrifugation[44]. For the Si NPs with rough surface (SNs-R), the obtained SNs-S were added to HF solution and kept stirring for 2 h. Subsequently, we obtained the SNs-R by washing and centrifugation.

For the synthesis of the polydopamine nanoparticles (PNs-S), 10 mg dopamine hydrochloride was added into 10 mL solution of Tris (20 mmol/L) and the solution was kept in stirring condition for 1 h at room temperature[45].

For the synthesis of polydopamine-coated silica nanoparticles with rough surface (PSNs-R), 10 mg dopamine hydrochloride and 100 μL SNs-R were added into 10 mL solution of Tris (20 mmol/L) at room temperature and kept in stirring condition for 1 h. Similarly, this method was also used to synthesize PSNs-S.

For loading JQ-1 into PSNs-R, 10 mg dopamine hydrochloride, 6 mg JQ-1 and 100 μL SNs-R were added into 10 mL 33% ethanol aqueous solution of Tris (20 mmol/L), after stirring for 4 h, we obtained JQ-1@PSNs-R.

The size and zeta potential of the nanoparticles mentioned above were measured by dynamic light scattering (Zetasizer ZEN3690, Malvern, UK). Transmission electron microscopy (Tecnai G2 F20 S-TWIN, FEI, Hillsboro, OH, USA) was used to characterize the morphology of the obtained nanoparticles. Atomic force microscope (Cypher VRS, Oxford, UK) and scanning electron microscope (Apreo S, Thermo Fisher Scientific, Waltham, MA, USA) were used to observe the surfaces of PNs-S, PSNs-S and PSNs-R. Kubo X1000 (Builder, Beijing, China) was used to conduct nitrogen adsorption−desorption experiments and calculate the surface area of PNs-S, PSNs-S and PSNs-R.

2.4. *Stability of JQ-1@PSNs-R*

JQ-1@PSNs-R solution was stored at room temperature for one week. The changes in nanoparticle size and zeta potential were monitored by dynamic light scattering.

2.5. Encapsulation efficiency and drug-loading rate of JQ-1@PSNs-R

The total amount of JQ-1 added during the preparation process was recorded as $W_{J\text{-}0}$. After synthesis, the reaction system was centrifuged. The supernatant was collected to analyze the amount of free JQ-1 by high-performance liquid chromatography (HPLC) and the amount of free JQ-1 was recorded as $W_{J\text{-}F}$. The prepared JQ-1@PSNs-R were weighed after lyophilization and recorded as W_{PSJ}. The encapsulation efficiency and drug-loading rate were calculated according to the Eqs. (1)–(4):

$$\text{Encapsulation efficiency}\ (\%) = (\text{Weight of drug in JQ-1@PSNs-R})/(\text{Weight of drug added}) \times 100 \quad (1)$$

$$\text{Encapsulation efficiency of JQ-1}(\%) = (W_{J\text{-}0} - W_{J\text{-}F})/W_{J\text{-}0} \times 100 \quad (2)$$

$$\text{Drug-loading rate}(\%) = (\text{Weight of drug in JQ-1@PSNs-R})/ \times (\text{Total weight of JQ-1@PSNs-R}) \times 100 \quad (3)$$

$$\text{Drug-loading rate of JQ-1}(\%) = (W_{J\text{-}0} - W_{J\text{-}F})/W_{PSJ} \times 100 \quad (4)$$

2.6. Release of JQ-1 from JQ-1@PSNs-R in vitro

To investigate the release kinetics profile of JQ-1 from JQ-1@PSNs-R, 1 mL of JQ-1@PSNs-R was placed into dialysis bags which the molecular weight cut-off was 3500 Da (Sigma, St. Louis, USA). Then, the dialysis bags were immersed into 20 mL PBS solutions with different pH containing 0.5% sodium dodecyl sulfate (SDS). The pH was set at 6.5 or 7.4 to simulate tumor microenvironment and normal humoral environment, respectively[46]. The dialysis bags were kept constant rotation at 37 °C. At different time points (0 h, 3 h, 6 h, 12 h, Days 1, 2, 3, 4, 5, 6, 7 and 8), the concentration of JQ-1 in the PBS solutions outside the dialysis bags were measured by HPLC.

2.7. Photothermal performance of SNs-R, PSNs-R and JQ-1@PSNs-R

SNs-R, PSNs-R and JQ-1@PSNs-R were suspended in deionized water and irradiated for 10 min using a near-infrared laser (Haoliangtech, Shanghai, China) at 808 nm with the power of 1.18 W/cm^2. PBS was set as the negative control. The temperatures of different solutions and PBS were recorded at different time points (0, 1, 3, 5 and 10 min) using an infrared thermal camera (Fotric 225, Shanghai, China).

The photothermal conversion performance of JQ-1@PSNs-R was also evaluated. JQ-1@PSNs-R was dispersed in water, and then irradiated with an 808 nm NIR laser at 1.18 W/cm^2. Pure water was used as a negative control. The temperature changes of JQ-1@PSNs-R and pure water were recorded. After irradiation for 300 s, the photothermal conversion efficiency (η) of JQ-1@PSNs-R can be calculated according to the Eq. (5).

$$\eta = (hA\,\Delta T_{max} - Q_s)/I(1 - 10^{-A\lambda}) \quad (5)$$

where I is the laser power, $A\lambda$ is the absorbance of JQ-1@PSNs-R at the wavelength of 808 nm, Q_s is the heat associated with the light absorbance of solvent, which is independent to be 25.2 mW. hA is unknown for calculation (h is the heat transfer coefficient, and A is the surface area of the container), but can be determined by the Eq. (6):

$$hA = -\frac{\sum_i m_i C_{p,i}}{t} \times Ln\frac{\Delta T}{\Delta T_{max}} \quad (6)$$

where m and $C_{p,i}$ are the mass and heat capacity of solvent (water), respectively. ΔT is the temperature change, which is defined as $T - T_{surr}$ (T and T_{surr} are the solution temperature and ambient temperature of the surroundings, respectively). ΔT_{max} is the temperature change at the maximum steady-state temperature.

2.8. The tumor cell protein adsorption capacity of polydopamine in vitro

B16F10 cells were collected and resuspended in water, and then cells were frozen and thawed repeatedly between liquid nitrogen and 37 °C. The cell lysate was then centrifugated at 10,000 rpm for 10 min with a high speed refrigerated centrifuge (3K15, Sigma, Roedermark, Germany), and the supernatant was collected as tumor cell protein. PLGA NPs, PNs-S, PSNs-S and PSNs-R were mixed with tumor cell protein, respectively, and the mixtures were kept constant rotation at 37 °C for 24 h. After incubation, the mixtures were centrifugated at 10,000 rpm for 10 min (3K15, Sigma, Roedermark, Germany) to obtain precipitates and resuspended with 0.2 mL water containing 0.1% Tween-80. After ultrasound and centrifugation, the supernatant was collected and the protein concentration was determined by a Pierce BCA Kit.

To analyze the adsorbed proteins on nanoparticles, SDS-PAGE experiment was conducted. PNs-S, PSNs-S and PSNs-R were incubated with B16F10 cells at 37 °C for 30 min, and then cells were irradiated with a near-infrared laser at 808 nm with the power of 1.18 W/cm^2 for 10 min. Then, the mixture was centrifuged at 1000 rpm for 1 min (3K15, Sigma, Roedermark, Germany) to remove cell debris, and the supernatant was centrifugated at 10,000 rpm for 10 min (3K15, Sigma, Roedermark, Germany) to obtain precipitates. The precipitates were resuspended with 0.2 mL water containing 0.25% Tween-80 and sonicated to dissociate the adsorbed proteins. To ensure the protein loading concentration of the samples, the dissociated proteins were concentrated. We transferred the dissociated proteins into a 1000 Da dialysis bag and 20 kDa PEG was on the outside the dialysis bag to absorb water. Finally, the dissociated tumor cell proteins from nanoparticles were further measured by SDS-PAGE.

2.9. Cytotoxicity of free JQ-1, SNs-R and JQ-1@PSNs-R

B16F10 cells were seeded in 96-well plates and incubated for 24 h. After exposed to free JQ-1 (15, 31, 62, 125 μg/mL), SNs-R (60, 120, 250, 500 μg/mL) and JQ-1@PSNs-R (54, 112, 225, 453 μg/mL) for 12 h, cells were added 100 μL fresh medium containing 10% CCK-8. After incubation at 37 °C for another 2 h, the absorbance of the solution at 450 nm was measured by a Varioskan Flash reader. The Eq. (7) was used to calculate the cell viability (%). The A_0, A_{treat} and $A_{control}$ represent the absorbance of blank medium, treated cells and untreated cells, respectively.

$$\text{Cell viability}\ (\%) = (A_{treat} - A_0/\,A_{control} - A_0) \times 100 \quad (7)$$

2.10. Cellular uptake of nanoparticles in vitro

DC 2.4 and B16F10 were seeded into 12-well plates and incubated for 24 h. After exposed to DID-labeled PNs-S, PSNs-S and PSNs-R for 2 h, the cells were collected and washed with PBS. Then, the cells were resuspended with 1 mL PBS solution and analyzed by flow cytometry (BD CytoFLEX, Franklin Lakes, USA).

2.11. Cellular uptake mechanisms of PNs-S, PSNs-S and PSNs-R in vitro

To investigate the mechanisms of these nanoparticles entering B16F10 cells, we conducted cellular uptake inhibition experiments. B16F10 were seeded into 12-well culture plates and pretreated with selective inhibitors of different internalization pathways at 37 °C for 1 h. After pretreatment, B16F10 cells were then exposed to DID-labeled PNs-S, PSNs-S and PSNs-R for another 1 h at 37 °C. To explore the effect of temperature on the uptake of nanoparticles, the experiments were also carried out at 4 °C. The cells were analyzed by flow cytometry. The inhibitors used in the experiments were as follows: amiloride (100×10^{-6} mol/L), methyl-β-cyclodextrin (10×10^{-6} mol/L), chlorpromazine (20×10^{-6} mol/L).

2.12. Interaction between B16F10 and nanoparticles of different roughness

The equivalent PSNs-R and PSNs-S were respectively dispersed in ethanol and transferred to the surface of Petri dishes. After evaporating the ethanol, the PSNs-R- and PSNs-S-coated Petri dishes were obtained. Equivalent B16F10 were seeded into the dishes and incubated for 1 h. After incubation, the dishes were shaken to discard the unattached cells. Then 2 mL PBS was added into the dishes, and the adherent cells were collected and counted. In order to accurately quantify the number of adherent cells, the collected B16F10 cells were lysed by 1 mL RIPA, and the total cell protein was quantified with a BCA Kit. The untreated Petri dish was set as the control group.

2.13. Inhibition of PD-L1 on B16F10 by JQ-1@PSNs-R in vitro

B16F10 cells were seeded into 12-well culture plates and incubated for 24 h. Then the cells were co-cultured with JQ-1@PSNs-R (at JQ-1 dosage of 30 μg/mL) for 3 or 5 h. Untreated cells and cells treated with free JQ-1 were set as control groups. After incubation, cells were collected and washed with PBS solution. The expression of PD-L1 in B16F10 cells was further analyzed by flow cytometry BD CytoFLEX.

2.14. Photothermal cytotoxicity in vitro

To assess photothermal cytotoxicity of PSNs-R, LDH (lactate dehydrogenase) cytotoxicity assay was carried out. B16F10 cells were seeded into 96-well culture plates and incubated for 24 h. After exposed to 100 μL PSNs-R (500, 250, 125, and 62.5 μg/mL) for 1 h, cells were irradiated for 10 min with a near-infrared laser (808 nm, 1.18 W/cm^2). Incubated for another 2 h, cells were measured by CytoTox 96® Non-Radioactive Cytotoxicity Assay Kit and cytotoxicity (%) was calculated according to the Eq. (8):

$$\text{Cytotoxicity (\%)} = (\text{Experimental group LDH release} / \text{Maximum LDH release}) \times 100 \quad (8)$$

B16F10 cells were incubated in 35 mm confocal dishes for 24 h. After incubation, cells were exposed to PSNs-R for 1 h and irradiated for 10 min with a near-infrared laser (808 nm, 1.18 W/cm^2). The cells were co-stained by fluorescein diacetate and propidium iodide, and then imaged by confocal laser scanning microscopy (Zeiss, Oberkochen, Germany).

2.15. Maturation and cytokine secretion of BMDCs in vitro

Bone marrow-derived dendritic cells (BMDCs) were isolated from healthy male C57BL/6 mice. After isolation, the BMDCs were seeded into 12-well plates and incubated for 6 h. Different formulations were added to BMDCs and incubated for 24 h. Lipopolysaccharide (LPS) and PBS were added as the positive control and negative control, respectively. The formulation "JQ-1@PSNs-R + L" was prepared as follows: B16F10 cells were seeded into 24-well plates and incubated with JQ-1@PSNs-R for 1 h. Then the B16F10 cells were irradiated for 5 min with a near-infrared laser (808 nm, 1.18 W/cm^2). Incubated for another 1 h, all components in the well were collected and centrifuged at 1000 rpm for 2 min (3K15, Sigma, Roedermark, Germany). And the supernatant was the formulation that added to BMDCs. After incubation, BMDCs were collected and co-stained with antibodies against CD80, CD86 and CD40, and then analyzed by flow cytometry. Cytokines in BMDCs culture supernatants were detected using an enzyme-linked immunosorbent assay (ELISA) Kit.

2.16. Inhibition of the PD-L1 expression in BMDCs in vitro

BMDCs were isolated from healthy male C57BL/6 mice. After isolation, the BMDCs were seeded into 12-well plates and incubated for 6 h. Tumor cells culture medium was collected and centrifuged at 2000 rpm for 3 min (3K15, Sigma, Roedermark, Germany). The supernatant would act as the tumor-related stimulants that added to BMDCs to stimulate cells expressing PD-L1. JQ-1@PSNs-R, JQ-1@PSNs-S or free JQ-1 was added to BMDCs and then cells were incubated with tumor-related stimulants at 37 °C for 5 h. After incubation, BMDCs were collected and co-stained with antibodies against CD11c and PD-L1, and then cells were analyzed by flow cytometry.

2.17. Photothermal therapy in vivo

B16F10 cells (1×10^6) were inoculated into the right flank of C57BL/6 mice to establish melanoma cancer models. Seven days later, when the tumor volumes were about 150 mm^3, free JQ-1 (5 mg/kg), PSNs-R (0.5 mg/mL, 100 μL), and JQ-1@PSNs-R (5 mg/kg for JQ-1) were intratumorally injected and then irradiated with a laser at 808 nm (1.18 W/cm^2) for 5 min. During the photothermal therapy, the temperature of the tumor was recorded at 0, 1, 3 and 5 min by an infrared thermal camera (Fotric 225).

2.18. Comparison of JQ-1@PSNs-S and JQ-1@PSNs-R in vivo

B16F10 cells were inoculated into the mice to establish melanoma cancer models. Seven days later, when the tumor volumes were about 150 mm^3, PBS, free JQ-1, JQ-1@PSNs-S, and JQ-1@PSNs-R (the dose of JQ-1 was 5 mg/kg) were intratumorally injected and then irradiated with a laser at 808 nm (1.18 W/cm^2) for 5 min. Three days after photothermal therapy, tumor tissues were collected and

the tumor cells and dendritic cells in the tissues were co-stained with antibodies to detect the PD-L1 expression by flow cytometry.

2.19. Expression reduction of PD-L1 on tumor cells in vivo

The day that mice received photothermal therapy was marked as Day 0. Mice were sacrificed on Day 7 after the photothermal therapy, and their tumors were collected. Ammonium-chloride-potassium lysing buffer was used to lyse red blood cells in tumors. Then the tumor cells were collected and co-stained with antibodies to detect PD-L1 expression by flow cytometry.

2.20. Lymphatic drainage after irradiation and immune responses in lymph nodes

C57BL/6 mice were inoculated with B16F10 cells (1×10^6) on the right flank to establish melanoma cancer models. When tumors grew to ~150 mm^3, DID-labeled PSNs-R (0.5 mg/mL, 100 μL) were injected into tumors and irradiated with a near-infrared laser (808 nm, 1.18 W/cm^2) for 5 min. Animals were sacrificed at 12, 24 and 48 h after irradiation and tumor-draining lymph nodes were harvested. The lymph nodes were imaged by Fluorescence Imaging System (Lumina III, PerkinElmer, Hopkinton, MA, USA). The dendritic cells and macrophages that internalized DID-labeled PSNs-R in lymph nodes were measured by flow cytometry.

C57BL/6 mice were established B16F10 melanoma cancer models. When tumors grew to ~150 mm^3, JQ-1@PSNs-R (the dose of JQ-1 was 5 mg/kg) were intratumorally injected and then irradiated with a near-infrared laser (808 nm, 1.18 W/cm^2) for 5 min. PBS, free JQ-1, laser only, JQ-1@PSNs-R only and PSNs-R + laser were set as contrasts. This time point was marked as Day 0. Animals were sacrificed on Day 7 and their axillary lymph nodes were prepared into single-cell suspension and co-stained with antibodies against CD11c, CD80, CD86 and CD40. Then the mature DCs were measured by flow cytometry.

2.21. Induced potent immune responses

After photothermal therapy, the mice were sacrificed on Day 7, and their spleens were collected. Splenocytes were suspended in ammonium-chloride-potassium lysing buffer to lyse red blood cells and the obtained immune cells were incubated in the medium containing 1 μL/mL brefeldin A and 200 μg/mL B16F10 cell lysate. After incubation, the cells were stained by antibodies and then measured by flow cytometry. The cytokine in the splenocytes supernatant and the IgG, IgG1 and IgG2a antibodies in blood serum were measured by ELISA Kits[47].

The mouse weight, tumor volume and the percent of mice alive were recorded every two days after photothermal therapy. After the photothermal therapy, mice were sacrificed on Day 14 and their tumors were collected and stained with hematoxylin and eosin for histological analysis.

To explore the ability of JQ-1@PSNs-R-mediated immune-photothermal therapy to prevent metastasis, we inoculated C57BL/6 mice with 1×10^6 B16F10 tumor cells on the left flank. After a week, this tumor was eliminated using photothermal therapy with JQ-1@PSNs-R, and then 1×10^5 B16F10 cells were inoculated on the right flank. Sizes of the left-flank and right-flank tumors were measured every two days.

2.22. Statistical analysis

All data were presented as mean ± SEM and graphed using Origin (Version 2017, OriginLab, Northampton, MA, USA) and GraphPad Prism (Version 8.0, La Jolla, CA, USA). One-way ANOVA followed by Tukey's multiple comparisons test and Two-way ANOVA were used for multiple comparisons. Significant differences were presented as follows: $^*P < 0.05$, $^{**}P < 0.01$, $^{***}P < 0.001$, $^{****}P < 0.0001$.

3. Results

3.1. Synthesis and characterization of SNs, PNs, PSNs and JQ-1@PSNs-R

Through the simple hydrolysis of TEOS and TSD in alkaline condition, we obtained Si NPs. Dynamic light scattering showed that the size of these synthesized smooth Si NPs (SNs-S) was 148.9 ± 2.4 nm, and the zeta potential was at −40.7 ± 0.4 mV (Table 1). After being etched by HF, these Si NPs (SNs-R) with rough surfaces had a decreased particle size (107.6 ± 2.3 nm). Through dopamine oxidation and self-polymerization, polydopamine was coated onto both kinds of Si NPs. The obtained polydopamine-coated smooth Si NPs (PSNs-S) had a size of 165.7 ± 2.8 nm with the zeta potential of −19.0 ± 0.4 mV, while the polydopamine-coated rough Si NPs (PSNs-R) showed an average size of 139.0 ± 6.4 nm and zeta potential of −21.4 ± 1.3 mV. Smooth polydopamine nanoparticles (PNs-S) serving as control were synthesized by dopamine oxidation and self-polymerization. After loading JQ-1, the average size of JQ-1@PSNs-R was 174.0 ± 2.4 nm while the zeta potential was −25.7 ± 0.7 mV.

The morphology of SNs-S, SNs-R and JQ-1@PSNs-R was further identified by transmission electron microscopy (TEM, Supporting Information Fig. S2). From TEM images, we found that compared with SNs-S, the SNs-R and JQ-1@PSNs-R had obvious rougher surfaces.

To characterize the roughness of different nanoparticles, transmission electron microscopy (TEM), scanning electron microscope (SEM) and atomic force microscope (AFM) were used. From the TEM (Fig. 1B) and SEM (Supporting Information Fig. S3) images of nanoparticles, we found that PSNs-R possessed more tortuous edge lines, while the edge lines of PNs-S and PSNs-S were smoother. Moreover, the 3D images of nanoparticles obtained by AFM also clearly showed that the surface of PSNs-R was much rougher than that of PNs-S and PSNs-S (Fig. 1C and D). We also calculated the average roughness (Ra) and the root mean square roughness (Rq) of PNs-S, PSNs-S and PSNs-R. Results showed that the Ra and Rq of PSNs-R were 14.880 nm and 17.600 nm, both of which were the largest among these three kinds of nanoparticles (Supporting Information Table S1). Nitrogen adsorption−desorption experiments were

Table 1 The characteristics of the nanoparticles.

Sample	Size (nm)	PDI	ζ potential (mV)
SNs-S	148.9 ± 2.4	0.144 ± 0.019	−40.7 ± 0.4
SNs-R	107.6 ± 2.3	0.087 ± 0.018	−43.7 ± 0.7
PNs-S	98.4 ± 3.1	0.078 ± 0.009	−31.7 ± 0.9
PSNs-S	165.7 ± 2.8	0.104 ± 0.027	−19.0 ± 0.4
PSNs-R	139.0 ± 6.4	0.061 ± 0.008	−21.4 ± 1.3
JQ-1@PSNs-R	174.0 ± 2.4	0.164 ± 0.019	−25.7 ± 0.7

Data were presented as mean ± SEM ($n = 3$). PDI, polydispersity distribution index.

conducted to calculate the surface area of PNs-S, PSNs-S and PSNs-R. All surface area calculation models showed that compared with PNs-S and PSNs-S, the PSNs-R had the largest surface area and this large surface area was caused by roughness rather than mesopores (Table 2 and Supporting Information Fig. S4). The BET surface area, Langmuir surface area and BJH adsorption cumulative surface area of PSNs-R were 59.6593, 68.1006 and 53.1278 m^2/g, respectively, which were significantly larger than those of other nanoparticles.

The encapsulation efficiency and loading capacity of JQ-1 for JQ-1@PSNs-R were 62.33 ± 0.58% and 27.59 ± 0.43%, respectively. The obtained JQ-1@PSNs-R exhibited good stability in water and in 10% FBS solution (Supporting Information Fig. S5). Moreover, the JQ-1@PSNs-R had pH-sensitive release characteristics, as the JQ-1 releasing profile showed that under pH of 6.5, the cumulative release of JQ-1 from nanoparticles was 59.25 ± 2.32% for 10 days, which was significantly faster than that under pH of 7.4 (Fig. 1E). Since polydopamine had little degradation *in vitro*, the release of JQ-1 from JQ-1@PSNs-R was relatively slower than that *in vivo*.

The photo-thermal conversion capability of nanoparticles was measured by infrared thermal camera (Fig. 1F and G). After laser irradiation (808 nm) for 10 min, the temperature of the solution containing PSNs-R or JQ-1@PSNs-R was increased by 28.76 ± 0.15 and 28.93 ± 0.06 °C, reaching a final to 58.37 and 58.60 °C, respectively. By calculation, the photothermal conversion efficiency (η) of JQ-1@PSNs-R was 43.78%.

3.2. Antigen adsorption capacity of polydopamine

As polydopamine contained many catechol groups, tumor lysates were prone to absorb onto nanoparticles after laser irradiation. To explore the antigen adsorption capacity of polydopamine-coated nanoparticles, PNs-S, PSNs-S and PSNs-R were mixed with tumor cell lysate, and the classic PLGA NPs group was set as the control. After the incubation and dissociation, the adsorbed tumor cell lysate proteins were collected and further measured by a Pierce BCA Kit. Results showed that polydopamine-coated nanoparticles had a stronger protein adsorption capacity than that of PLGA NPs, as the proteins dissociated from PNs-S, PSNs-S and PSNs-R were 2.7-, 2.8- and 3.1-fold higher than that from PLGA NPs (Fig. 1H).

To investigate the ability of the nanoparticles to adsorb tumor cell antigens after photothermal therapy, we simulated the adsorption of tumor antigens by nanoparticles *in vitro*. Nanoparticles incubated with B16F10 cells were collected after laser irradiation, and the protein components adsorbed by the nanoparticles after photothermal therapy were analyzed by the SDS-PAGE experiment. By comparing the bands of the cell lysate group, we found that the polydopamine-coated nanoparticles adsorbed rather comprehensive tumor protein antigens (Fig. 1I).

3.3. Rough surface markedly elevated the cellular uptake level of nanoparticles

The internalization of nanoparticles with different roughness on B16F10 and DC 2.4 were evaluated (Fig. 2A). On B16F10 cells, compared with PSNs-S, the uptake efficiency of PSNs-R was significantly increased from 13.8% to 86.7%, and the uptake efficiency of the PNs-S was only 10.2%. On DC 2.4 cells, the rough surface also mediated higher cellular uptake. The uptake efficiency of PNs-S and PSNs-S on DC 2.4 cells were only 19.2% and 23.0%, respectively, while the uptake efficiency of PSNs-R reached to 96.3%.

To find out the underlying mechanisms of the internalization of these nanoparticles, the experiments were carried out in the presence of different endocytic pathway inhibitors. Results suggested that the internalization of PNs-S on B16F10 cells was related to micropinocytosis-, cholesterol- and clathrin-mediated endocytosis (Fig. 2B). Interestingly, when the polydopamine was coated on silica nanoparticles, they were mainly internalized by B16F10 cells *via* clathrin-mediated endocytosis, no matter their surface was smooth or rough. Besides, all internalizations of these nanoparticles were significantly inhibited at 4 °C, suggesting that these internalizations were energy-dependent processes.

We further explored the mechanisms for the higher uptake efficiency of PSNs-R. We firstly hypothesized that the serum proteins were adsorbed on the surface of the nanoparticles, which may help the entry of the nanoparticles into the B16F10 cells. However, results showed that in the presence of serum, the uptake of PSNs-R and PSNs-S on B16F10 cells were both decreased (Supporting Information Fig. S6). Next, we speculated that the rough surface of PSNs-R made it easy to adhere to B16F10 cells. We prepared PSNs-R- and PSNs-S-coated Petri dishes and investigated the interaction between B16F10 cells and the nanoparticles within 1.5 h[48]. Results showed that (10.22 ± 0.05) × 10^5 cells adhered to the surface of PSNs-R-coated dishes, while only (8.69 ± 0.09) × 10^5 cells adhered to the surface of PSNs-S-coated dishes, indicating a stronger affinity between B16F10 cells and the nanoparticles with rough surface (Fig. 2D). This conclusion was further confirmed by quantifying the protein of the adherent cells on the Petri dishes. The total protein of adherent cells on PSNs-R-coated dishes was 1078.08 ± 4.97 μg, which was significantly higher than that of PSNs-S-coated dishes (836.13 ± 6.81 μg, Fig. 2D).

Although the rough surface was conducive to the cellular internalization, rough-surface nanoparticles showed good safety. To quantify the cytotoxicity of JQ-1@PSNs-R, SNs-R and free JQ-1, mouse melanoma B16F10 tumor cells were incubated with different formulations. When cells were exposed to free JQ-1 and JQ-1@PSNs-R at the same JQ-1 dose (31 μg/mL), the cell viabilities were 55.66% and 83.48%, respectively. Surprisingly, compared with JQ-1@PSNs-R, the cytotoxicity of free JQ-1 was higher (Fig. 2E). Additionally, there was no obvious cytotoxicity observed for SNs-R, as the cell viability was 95.13% when the concentration of SNs-R even reached to 250 μg/mL.

The PD-L1 downregulation in B16F10 cells by JQ-1 was measured by flow cytometry. Compared with free JQ-1, the JQ-1@PSNs-R could inhibit PD-L1 expression to a much lower level. The PD-L1 expression in B16F10 cells dramatically decreased to 10.5% with only 3 h of exposure to JQ-1@PSNs-R (Fig. 2F). We speculated that in the internalization process of JQ-1@PSNs-R, nanoparticles entered cells *via* clathrin-mediated endocytosis, and then they would be transferred to cytoplasm or lysosomes by endocytic vesicles. After polydopamine degradation in cells, the JQ-1 would be released from nanoparticles and take effect to inhibit PD-L1 expression.

3.4. In vitro photothermal toxicity and immunostimulatory activity

The LDH cytotoxicity assay was carried out to assess the photocytotoxicity of PSNs-R. With laser irradiation (808 nm) for 5 min, PSNs-R (500 μg/mL) effectively destroyed 67.4% of tumor cells

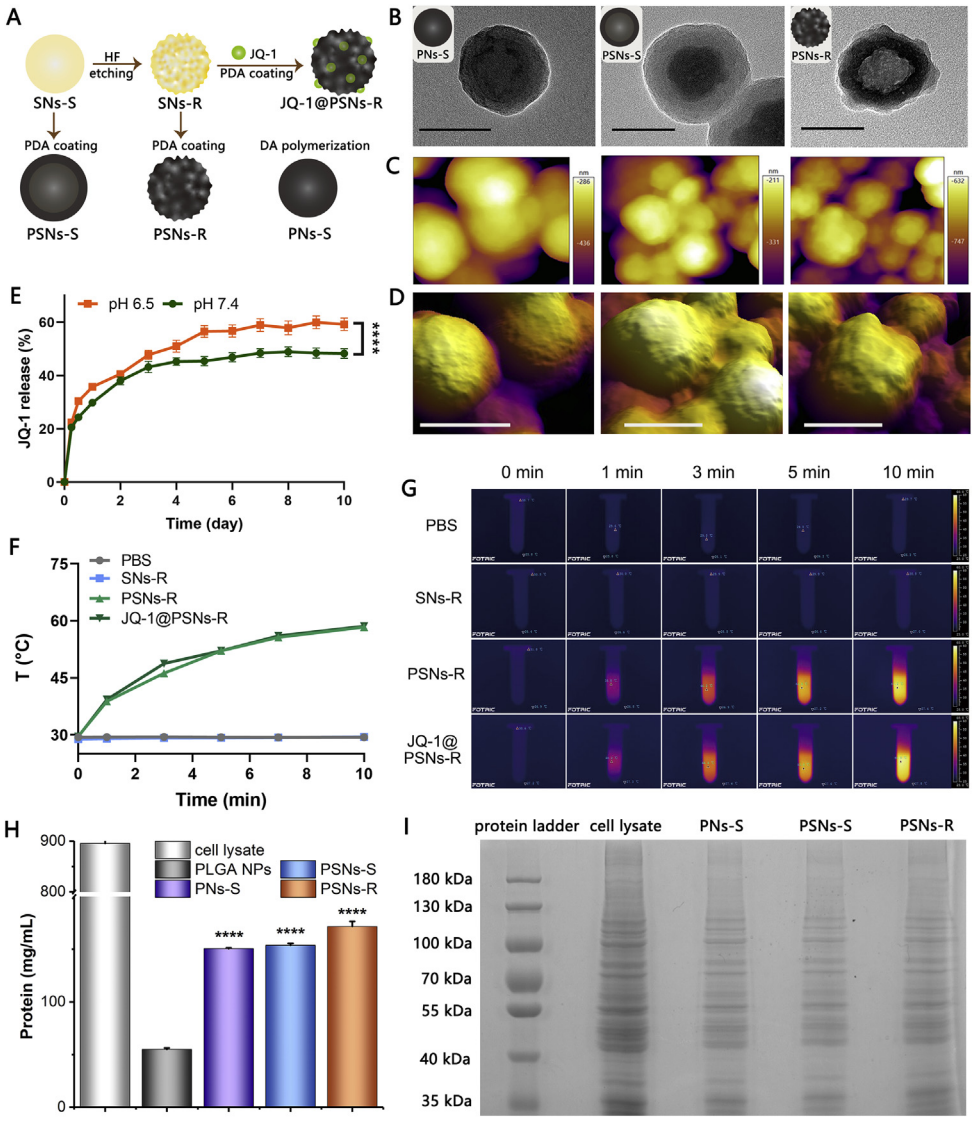

Figure 1 Characterization of nanoparticles. (A) Schematic illustration of basic preparation steps and nanoparticles. (B) Transmission electron microscopy images of PNs-S, PSNs-S and PSNs-R. Scale bar = 100 nm. (C) Atomic force microscopy images of PNs-S, PSNs-S and PSNs-R. (D) The 3D images of PNs-S, PSNs-S and PSNs-R. Scale bar = 100 nm. (E) Released JQ-1 from JQ-1@PSNs-R under different pH conditions (data were mean ± SEM, $n = 3$ and analyzed by two-way ANOVA. $^{****}P < 0.0001$). (F) Temperature rise curves of PBS, SNs-R, PSNs-R and JQ-1@PSNs-R after 808 nm laser irradiation. (G) Photo-thermal conversion capacity of PBS, SNs-R, PSNs-R and JQ-1@PSNs-R. (H) The ability of PLGA NPs, PNs-S, PSNs-S and PSNs-R to adhere to cell lysate (data were mean ± SEM, $n = 4$ and analyzed by one-way ANOVA. $^{****}P < 0.0001$). (I) The SDS-PAGE result to show the adsorbed protein components of PNs-S, PSNs-S and PSNs-R.

(Fig. 2G). This photothermal toxicity of the nanoparticles was further confirmed by confocal microscopy images (Fig. 2H and Supporting Information Fig. S7). The images showed that after photothermal treatment, most of the cells were killed, while the cytotoxicity was not observed in other groups.

BMDCs maturation experiments could effectively demonstrate the immune stimulation effect of the formulations on DCs. We isolated BMDCs from healthy male C57BL/6 mice, and the immune-stimulating effect of photothermal treatment on BMDCs maturation was simulated *in vitro* as described in methods. Briefly, B16F10 cells were incubated with JQ-1@PSNs-R, and after incubation, cells were irradiated for 5 min with a near-infrared laser (808 nm, 1.18 W/cm^2). Then the intact cells were removed and the obtained supernatant was added to BMDCs. The expression of $CD80^+$ $CD40^+$ and $CD86^+$ $CD40^+$ in BMDCs that stimulated by "JQ-1@PSNs-R + L" was elevated by 8.49- and 2.8-fold than that of the PBS-treated group, respectively (Fig. 3B and C). The ELISA results proved that the IL-6 and TNF-α secreted in JQ-1@PSNs-R + L group was elevated by 186- and 6.5-fold compared with that in the PBS group, indicating that JQ-1@PSNs-R + L had excellent immune activation ability (Fig. 3D).

Based on the reported research, PD-L1 is not only expressed in tumor cells, but also in DCs[49]. Importantly, the expression of PD-L1 in DCs can significantly affect the ability of mature DCs to activate T cells, and then inhibit the anti-tumor immunity. Since the JQ-1@PSNs-R had a high uptake in DCs, we speculated that the JQ-1@PSNs-R could also reduce the expression of PD-L1 in DCs, and thus better activated the immune responses. We tested the ability of the JQ-1@PSNs-R to reduce the

Table 2 The characteristics of roughness of the nanoparticles surface.

Sample	BET surface area (m^2/g)	Langmuir surface area (m^2/g)	BJH adsorption cumulative surface area (m^2/g)
PNs-S	43.7657	54.7633	33.6204
PSNs-S	40.5296	48.0090	24.6020
PSNs-R	59.6593	68.1006	53.1278
JQ-1@PSNs-R	55.2503	64.8606	52.4467

BET, Brunauer–Emmett–Teller method; BJH, Barret–Joyner–Halenda method.

expression of PD-L1 in BMDCs (Supporting Information Fig. S8). Surprisingly, JQ-1@PSNs-R showed an excellent inhibiting effect. Compared with the control group which was only treated with tumor-related stimulants, the JQ-1@PSNs-R reduced the expression of PD-L1 by 51.6%, which performed much better than the free JQ-1 group (7.3%) and JQ-1@PSNs-S group (34.6%).

3.5. *Photothermal-mediated immunotherapy in vivo*

To confirm the photothermal conversion efficiency of nanoparticles *in vivo*, mice bearing B16F10 tumors that grew to approximately 150 mm^3 were intratumorally injected with 100 μg PSNs-R or JQ-1@PSNs-R and irradiated with a near-infrared laser for 5 min at tumor sites. The temperature of tumors rose to 56.9 or 56.6 °C, which could effectively destroy tumors (Fig. 4B).

To examine whether JQ-1@PSNs-R could effectively down-regulate the expression of PD-L1 in tumor cells *in vivo*, at 7 days after therapy, the residual tumor tissues were harvested and the PD-L1 expression level was determined. Our results showed that the administration of free JQ-1 significantly decreased the PD-L expression from 65.5% to 30.6% as compared with PBS group. When the JQ-1 was loaded in JQ-1@PSNs-R, the PD-L1 expression on tumor cells was further suppressed to 20.1%. Moreover, after treated with JQ-1@PSNs-R-mediated photothermal therapy (JQ-1@PSNs-R + L), the PD-L1 expression level on tumor cells decreased to only 9.6% (Fig. 4C). These results showed that JQ-1@PSNs-R could not only destroy tumors directly by photothermal therapy but effectively down-regulate the expression of PD-L1, indicating that the immunosuppressive microenvironment of tumor sites was effectively altered.

3.6. *Potent immune responses induced by JQ-1@PSNs-R*

The *in vitro* experiments showed that the enhanced surface roughness helped nanoparticles enter cells. To confirm this effect *in vivo*, we also compared the PD-L1 inhibition effect of JQ-1@PSNs-S and JQ-1@PSNs-R in tumor-bearing mice (Supporting Information Figs. S9 and S10). We evaluated the expression of PD-L1 in tumor cells and dendritic cells after intratumoral injection of JQ-1@PSNs-R and JQ-1@PSNs-S. The results showed that the PD-L1 expression of tumor cells in the JQ-1@PSNs-R group was only 26.5 ± 3.1%, while that of JQ-1@PSNs-S group was 34.7 ± 6.5%, indicating JQ-1@PSNs-R had a better PD-L1 inhibiting effect than JQ-1@PSNs-S. Therefore, we screened out the rough-surface nanoparticles loaded with JQ-1 as the optimal formulation to be used in the further animal experiments of immuno-photothermal combined therapy against tumors. To examine whether the photothermal therapy in the tumor site could induce a subsequent immune response, we carried out a series of experiments.

After intratumoral injection and laser irradiation, the tumor-draining lymph nodes were harvested at 12, 24 and 48 h to investigate the percentage of antigen-adsorbed nanoparticles reaching the lymph nodes. The fluorescence imaging results showed that as time prolonged, the accumulation of DID-labeled PSNs-R in lymph nodes increased (Fig. 5B). Flow cytometry results suggested that this accumulation was not only passive drainage but endocytosed by DCs and macrophages in lymph nodes (Fig. 5C and D).

To study the immune-stimulating effects of the photothermal combined immunotherapy *in vivo*, we analyzed the maturation of DCs in lymph nodes after 7 days of photothermal therapy. Results showed that compared with PBS group, the proportion of $CD40^+$ $CD86^+$ and $CD40^+$ $CD80^+$ DCs increased by 9.1% and 0.24% in JQ-1@PSNs-R + L group, respectively, indicating the photothermal-mediated immunotherapy led to significantly higher maturation of DCs in lymph nodes (Fig. 5E).

Encouraged by the results of mature DCs in the lymph nodes, we further investigated the proportion of antigen-specific T cells in spleens. The spleens of mice on Day 7 after immuno-photothermal therapy were harvested, and the proportions of tumor antigen-specific $CD4^+$ helper T lymphocytes and $CD8^+$ cytotoxic T lymphocytes were determined (Fig. 6B and Supporting Information Fig. S11). Results showed that there was no significant difference between PBS group, free JQ-1 group and laser-only group in the results of proportions of tumor-antigen specific T lymphocytes. However, compared with PBS-treated group, mice treated with JQ-1@PSNs-R and laser irradiation (JQ-1@PSNs-R + L) produced significantly elevated $CD8^+$ cytotoxic T lymphocytes and $CD4^+$ helper T lymphocytes, which were 2.17- and 4.8-fold higher than that in PBS-treated mice, respectively.

Since antibodies and cytokines had a certain auxiliary role in anti-tumor therapy, we tested them after immune-photothermal therapy. As expected, mice treated with JQ-1@PSNs-R and laser irradiation (JQ-1@PSNs-R + L) also had stronger serum antibodies and cytokines. The tumor antigen-specific IgG, IgG1 and IgG2a in serum, compared with that in PBS group, increased by 1.7-, 4.3- and 6.0-fold respectively (Fig. 6C). Moreover, the secreted IFN-γ in culture supernatant of splenocytes also increased by 8.1-fold (Fig. 6D), indicating the validity of this photothermal-mediated immunotherapy.

Survival experiments could effectively prove the tumor-killing and anti-metastasis effects of the therapy. The result showed that mice in PBS group, free JQ-1 group and laser-only group all died within 15 days after tumor inoculation. Although mice treated with PSNs-R and laser irradiation (PSNs-R + L) had a longer survival time, they all died within 21 days. Surprisingly, 66.67% of mice treated with JQ-1@PSNs-R and laser irradiation (JQ-1@PSNs-R + L) survived at least 50 days in a tumor-free state (Fig. 6E and F). To visualize the recovery of mice after photothermal immunotherapy, we photographed one mouse at different

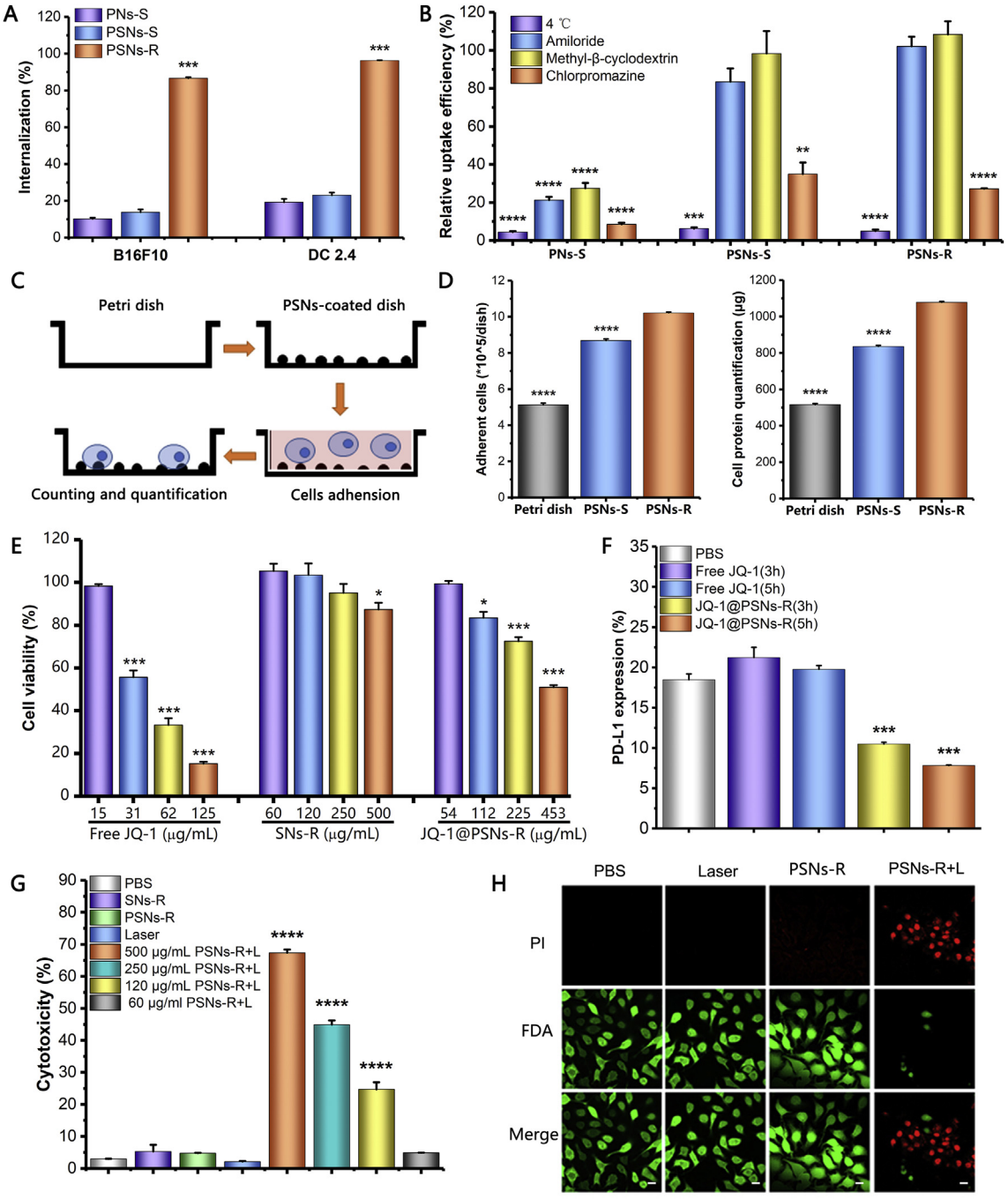

Figure 2 Internalization, cytotoxicity and PD-L1 inhibition effect of JQ-1@PSNs-R *in vitro*. (A) Internalization of PNs-S, PSNs-S and PSNs-R on B16F10 cells and DC2.4. (B) Relative uptake efficiency of PNs-S, PSNs-S and PSNs-R on B16F10 cells at 4 or 37 °C with amiloride, methyl-*β*-cyclodextrin or chlorpromazine. (C) Diagrammatic sketch about investigating the interaction between B16F10 cells and PSNs. (D) The quantification results of B16F10 cells that adhered to Petri dish, PSNs-S-coated dish and PSNs-R-coated dish. (E) Cytotoxicity of free JQ-1 (15, 31, 62, 125 μg/mL), SNs-R (60, 120, 250, 500 μg/mL) and JQ-1@PSNs-R (54, 112, 225, 453 μg/mL). (F) The PD-L1 inhibition effects of free JQ-1 (30 μg/mL) and JQ-1@PSNs-R (108 μg/mL) in B16F10 cells. (G) LDH results showed the cytotoxicity of SNs-R, PSNs-R, laser and PSNs-R + L in B16F10 cells; (H) Confocal fluorescence microscopy images of live (green) and dead (red) B16F10 cells after photothermal therapy. Propidium iodide and fluorescein diacetate were used to stain dead and live cells. Scale bar = 10 μm. Data were mean ± SEM, $n = 3–5$ and analyzed by one-way ANOVA. *$P < 0.05$, **$P < 0.01$, ***$P < 0.001$ and ****$P < 0.0001$.

time points with a digital camera (Fig. 6G). The results showed that the laser-irradiated spots would scab, but the skin returned to normal after the scab fell off. Besides, this JQ-1@PSNs-R-mediated photothermal therapy was also safe, as the results of mice weight, organs and blood routine test were normal (Supporting Information Figs. S12–S14).

In addition to intuitive tumor volume and survival data, we also evaluated the ability of immuno-photothermal combined therapy

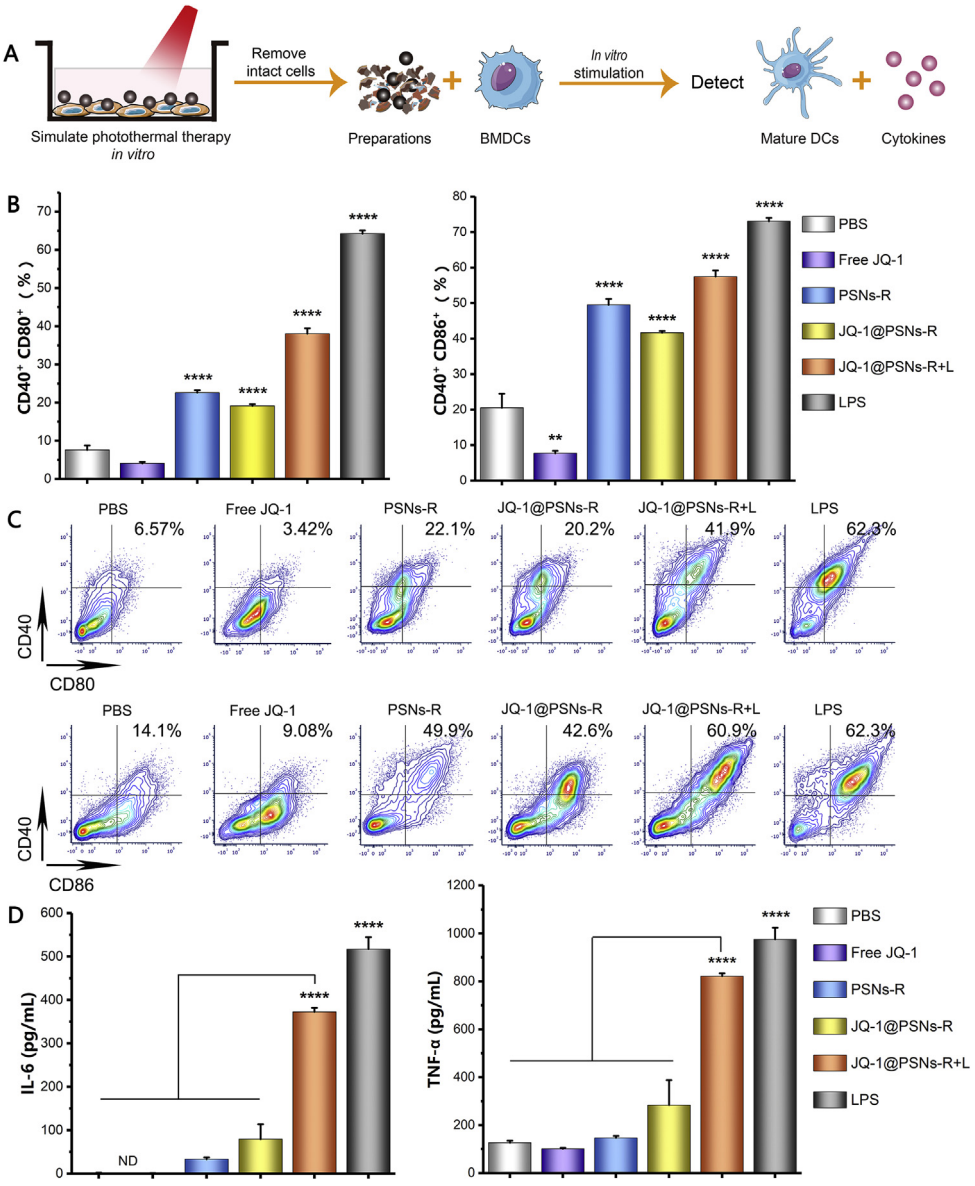

Figure 3 Maturation of BMDCs induced by JQ-1@PSNs-R + L. (A) Schematic illustration of the process of obtaining preparations, stimulating BMDCs and detections. (B) Percentage of mature BMDCs after stimulation. (C) Contour map of flow cytometry results of mature BMDCs. (D) After preparations stimulation, the cytokines secreted by BMDCs were tested by ELISA kits. Compared with PBS, Free JQ-1, PSNs-R and JQ-1@PSNs-R, the IL-6 and TNF-α secretion levels of JQ-1@PSNs-R + L were significantly increased. Data were mean ± SEM, $n = 4$ and analyzed by one-way ANOVA, $^{**}P < 0.01$ and $^{****}P < 0.0001$.

of JQ-1@PSNs-R to prevent tumor recurrence and metastasis. Mice bearing B16F10 tumors that had grown to approximately 150 mm^3 were intratumorally injected with different formulations and treated with or without near-infrared laser. Histology of tumor tissue at 14 days after photothermal therapy showed that JQ-1@PSNs-R-mediated immune-photothermal therapy (JQ-1@PSNs-R + L) destroyed tumor cells and successfully prevented the tumor from recurring. However, the slice images of other groups showed that mice all had varying degrees of tumor tissue (Fig. 6H). The bilateral melanoma model of C57BL/6 mice was also established to explore the ability of JQ-1@PSNs-R + L to prevent metastasis. After the first tumor eliminated by photothermal therapy with JQ-1@PSNs-R, the second tumor was inoculated on the right flank. Sizes of the left- and right-flank tumors were measured every two days and the results showed that JQ-1@PSNs-R + L led to the slowest growth of both (Supporting Information Fig. S15).

4. Discussion

In this research, we constructed photothermal convertible nanoparticles to deliver a BRD4 inhibitor into tumor cells. By combining photothermal therapy with immunotherapy, we have successfully eliminated melanoma and prevented tumor recurrence. Importantly, by increasing the surface roughness of the nanoparticles, we have

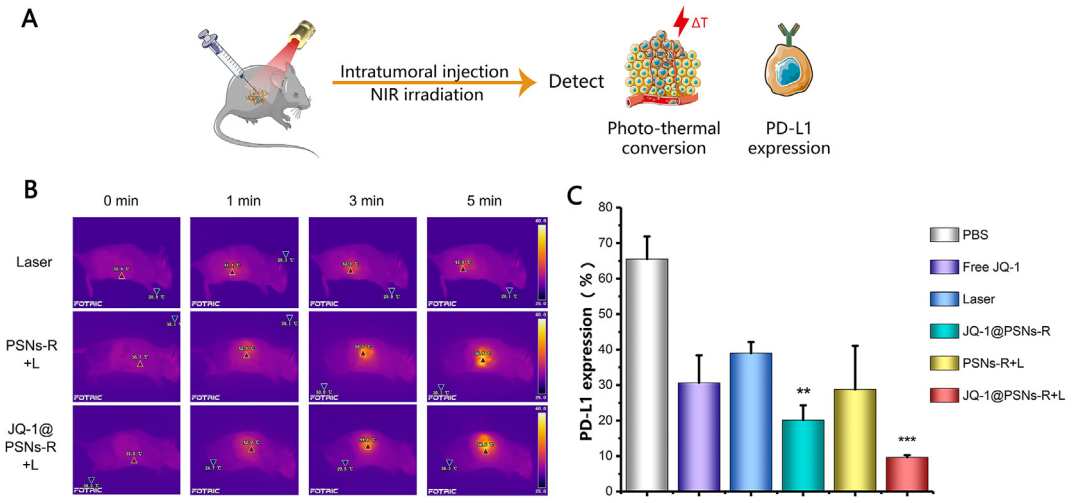

Figure 4 The therapeutic efficacy of JQ-1@PSNs-R + L on mouse tumors. (A) Schematic illustration of immunotherapy combined photothermal therapy and the detections. (B) Photo–thermal conversion effects of PSNs-R and JQ-1@PSNs-R *in vivo*. (C) The inhibition of PD-L1 expression in tumor cells. Data were mean ± SEM, $n = 4$ and analyzed by one-way ANOVA, $^{**}P < 0.01$ and $^{***}P < 0.001$.

significantly improved the cellular uptake efficiency of the nanoparticles, resulting in an improved therapeutic effect.

Nanomedicines are playing more and more important roles in treating various diseases. It has been reported that the physical properties of nanoparticles such as size[16,17], shape[17–20], surface charge[21,22], hydrophobicity[23,24] and stiffness could have significant influences on their *in vivo* delivery efficacy. Nevertheless, the idea of increasing the surface roughness of the nanoparticles to elevate cellular internalization and strengthen therapeutic effects is novel and rarely reported, as it is hard to use the same material to prepare nanoparticles with different surface roughness. Here, we exploited a facile method to prepare nanoparticles with different surface roughness of the same material. Firstly, we simply etched organic-inorganic hybrid silica nanoparticles to remove the organic part and obtain rough silica nanoparticles. After coating rough and smooth silica nanoparticles with polydopamine, we successfully obtained nanoparticles with the same polydopamine material but with different roughness, which was of great significance for studying the effect of surface roughness on cells. We used multiple methods to characterize the roughness of nanoparticles. As images (Fig. 1B and D) and data (Table 2) showed, PSNs-R had more uneven surfaces and larger surface area than PSNs-S. Then, we looked into their uptake behaviors on B16F10 and DC 2.4 cells. Results (Fig. 2A) proved that the increased roughness of nanoparticles significantly improved the ability to enter cells, indicating nanoparticles with rough surfaces were good platforms for drug delivery.

We further studied the mechanism of rough surface promoted cellular uptake. Inspired by the adhesion characteristics of cells to different substrates during the tissue culture process[48], we used nanoparticles with different roughness to coat on the Petri dishes, and calculated the number of cells that adhere to the surface in a short period of time to characterize the ability of cells to grasp nanoparticles. Compared with PSNs-S-coated surface, results (Fig. 2D) showed cells prefer to adhere to PSNs-R-coated surface, indicating there was higher affinity between cells and nanoparticles with rough surface of nanoparticles. As Fig. 2B suggested, PSNs entered B16F10 cells *via* clathrin-mediated endocytosis (CME). During the CME process, several accessory proteins, including amphiphysin, endophilin, epsin and dynamin, will induce membrane curvature by asymmetrically inserting into the outer lipid monolayer to form endocytic vesicles[50]. Based on this, we speculated that due to the asymmetry of surface, the PSNs-R themselves provided a motive power to induce membrane curvature and reduced the energy of CME process.

Immunotherapy is one of the most commonly used therapies in combination with photothermal therapy to eradicate tumors, and to activate the immune system, some steps are critical[42]. First, DCs have to take up antigens and migrate to lymph nodes; then, the DCs need to mature in lymph nodes; finally, mature DCs successfully present antigens to T cells. In our research, it is difficult to characterize whether the generated tumor antigens are internalized by DCs. However, we confirmed that PSNs-R can absorb tumor antigens after laser irradiation *in vitro* (Fig. 1H), and the flow cytometry results showed that PSNs-R can be successfully internalized by DCs and be carried to lymph nodes after intratumoral injection and photothermal therapy (Fig. 5C). Based on the above results we can reasonably infer that the tumor antigens are internalized by DCs and they migrate to the draining lymph nodes together, completing the first step in activating the immune response. In the second step, after uptake antigens, DCs have to mature before presenting antigens to T cells. To prove this, we collected lymph nodes and stained the DCs with antibodies against mature molecules after therapy. The proportion of mature DCs in the mice who received JQ-1@PSNs-R-based immuno-photothermal therapy was significantly increased (Fig. 5E), providing a guarantee for DCs to present antigens to T cells. As the most crucial step, to confirm that mature DCs presented antigens to T cells and activated T cell responses successfully, we evaluated the tumor antigen-specific T cell responses (Fig. 6B). As expected, the results showed that mice treated with JQ-1@PSNs-R and laser irradiation produced significantly elevated tumor-antigen specific $CD8^+$ cytotoxic and $CD4^+$ helper T lymphocytes, which indicated the activation of the tumor-specific cellular immune response. Moreover, JQ-1@PSNs-R-mediated photothermal therapy also

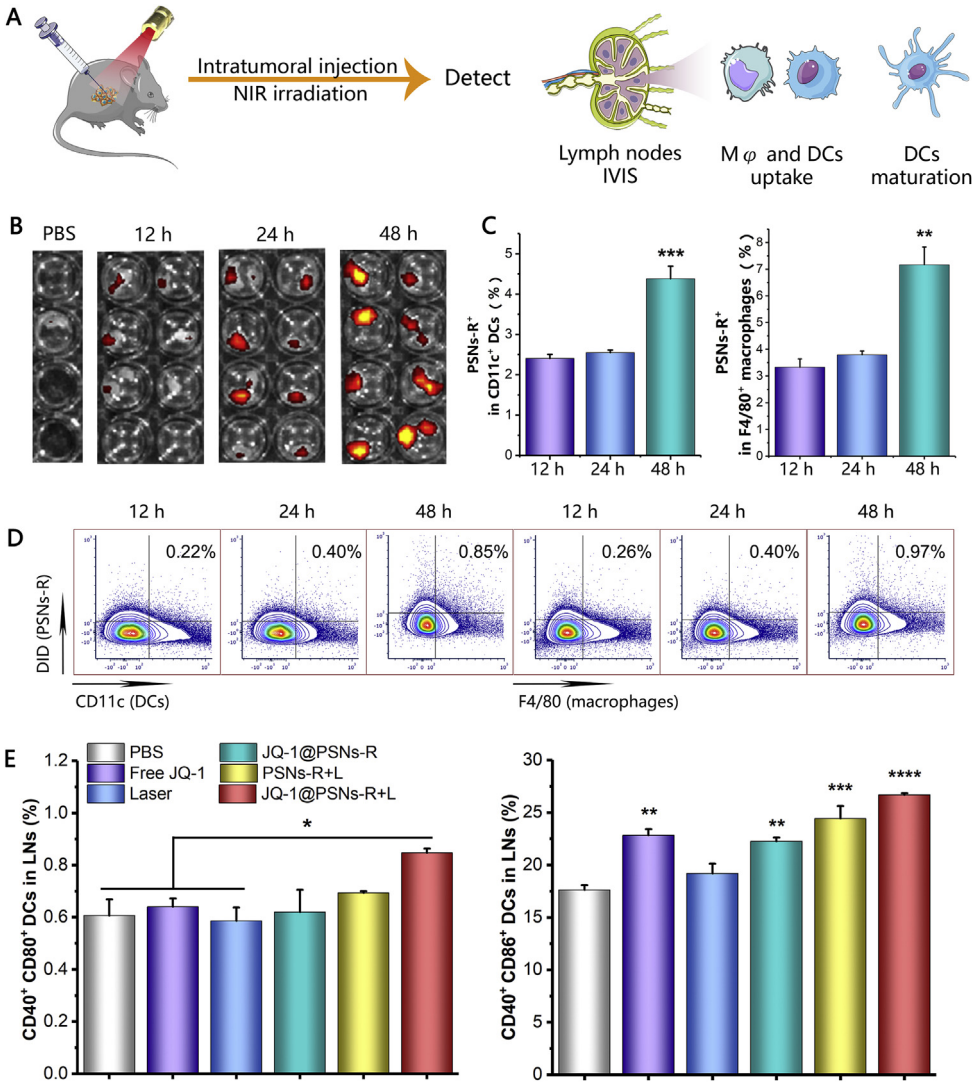

Figure 5 The immune responses induced by JQ-1@PSNs-R + L in mice lymph nodes. (A) Schematic illustration of immunotherapy combined photothermal therapy and the detections (B) *Ex vivo* imaging of lymph nodes at 12, 24, and 48 h after photothermal therapy. (C) The percentage of PSNs-R$^+$ macrophages and PSNs-R$^+$ DCs in lymph nodes at different time points after photothermal therapy. (D) Contour map of flow cytometry results of PSNs-R$^+$ macrophages and PSNs-R$^+$ DCs in lymph nodes. (E) Mature DCs in lymph nodes after therapy. Data were mean ± SEM, $n = 3$–4 and analyzed by one-way ANOVA, $^*P < 0.05$, $^{**}P < 0.01$, $^{***}P < 0.001$ and $^{****}P < 0.0001$.

successfully elevated tumor antigen specific-antibodies in serum, and this humoral immune response would play a good auxiliary effect on cellular immunity.

In addition to activating the immune response, it is also very important to relieve the immune suppression of the tumor microenvironment. Recently, intravenous administration of immune checkpoint inhibitors has led to increased long-term survival in cancer patients[51,52]. However, this systemic drug administration not only leads to poor drug exposure to the tumor[53], but also more likely to cause systemic toxicity[54,55]. Therefore, we adopted intratumoral injection as the way for JQ-1@PSNs-R administration[56]. Compared with other nanoparticles and systemic administration, the biodegradable and biocompatible properties of polydopamine layer provided sustained drug release and this intratumoral injection reduced the dosage and the frequency of administration[57]. During the entire treatment, mice received only one dosage of JQ-1@PSNs-R. Compared with multiple systemic administration of PD-L1 inhibitors commonly reported in the literature, this designed strategy was much more convenient, which could increase patient compliance. After intratumoral injection of JQ-1@PSNs-R, we analyzed the expression of PD-L1 in tumor cells, and results showed that JQ-1@PSNs-R-mediated photothermal therapy had an excellent ability to down-regulate the expression of PD-L1 (Fig. 4C). Moreover, since JQ-1@PSNs-R could be internalized by both tumor cells and DCs (Fig. 2A), we speculated that JQ-1@PSNs-R could not only reduce the expression of PD-L1 in tumor cells but also in DCs. As expected, the results confirmed our speculation (Supporting Information Fig. S10). Consequently, this intratumoral injection of JQ-1@PSNs-R not only changed the immunosuppressive microenvironment in the tumor site but amplified the effect of the immune system, which significantly improved the antitumor responses. Thus, we reasonably speculated that this reduced-dose single administration of JQ-1@PSNs-R could reduce treatment-induced toxicity and cause fewer immune side effects.

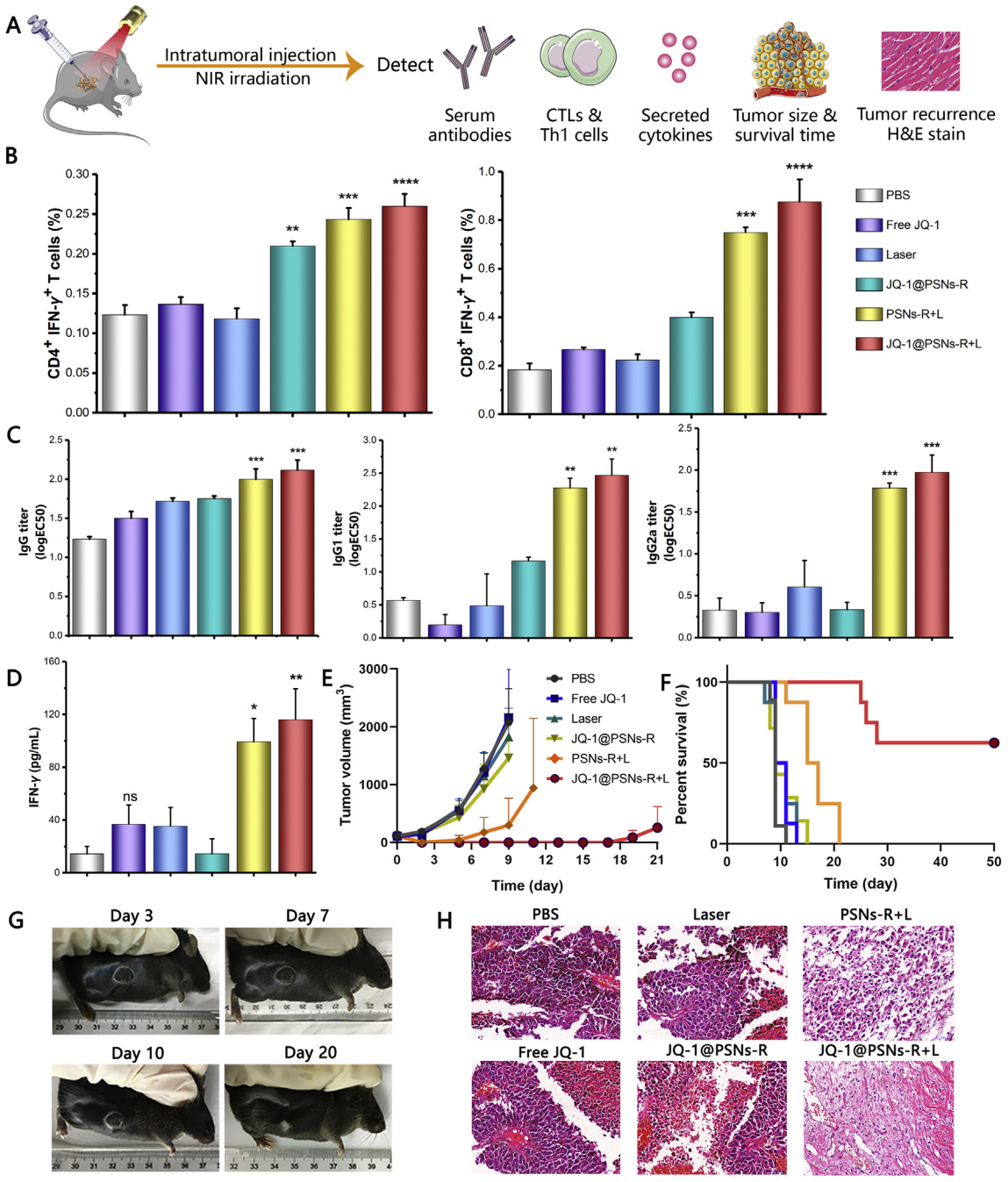

Figure 6 Systemic anti-tumor immune responses and tumor growth inhibition potency triggered by JQ-1@PSNs-R-based photothermal-mediated immunotherapy. (A) Schematic illustration of photothermal-mediated immunotherapy and the detections. (B) Percentages of $CD4^+$ IFN-γ^+ T cells (Th1 cells) and $CD8^+$ IFN-γ^+ T cells (CTLs) in spleens. (C) Antigen-specific IgG, IgG1 and IgG2a in serum. (D) IFN-γ secreted by splenocytes. (E) Tumor growth after photothermal-mediated immunotherapy (8 mice per group). (F) Survival of mice after photothermal-mediated immunotherapy (8 mice per group). (G) Images of scab healing of the same mouse after photothermal-mediated immunotherapy; (H) Images of hematoxylin-eosin stained tumor sections to confirm the prevention of tumor recurrence and metastasis after photothermal-mediated immunotherapy (HE stain, × 400). Data were mean ± SEM, $n = 3$–4 and analyzed by one-way ANOVA. $^*P < 0.05$, $^{**}P < 0.01$, $^{***}P < 0.001$ and $^{****}P < 0.0001$. ns, not significant.

5. Conclusions

In summary, we have engineered a dual functional drug delivery system that could achieve a synergistic anti-tumor effect by combining photothermal therapy and immunotherapy. Based on our findings, the increased surface roughness of polydopamine nanoparticles significantly elevated cellular internalization. Taking the advantage of higher uptake of rough-surface nanoparticles, we encapsulated JQ-1 into nanoparticles and potently induced inhibition of PD-L1 in tumor cells and DCs. In general, our nanoparticles successfully destroyed tumors *via* photothermal therapy and further activated tumor-specific immune responses against

residual tumor cells. In further studies, the high drug-loading and intracellular uptake properties of this drug delivery system could be utilized for treating other diseases.

Acknowledgements

We acknowledge the financial support of the National Natural Science Foundation of China (Nos. 81925036 & 81872814), the Science & Technology Major Project of Sichuan Province (No. 2018SZDZX0018, China), the Key Research and Development Program of Science and Technology Department of Sichuan Province (No. 2020YFS0570, China), 111 project (No. b18035, China) and the Fundamental Research Funds for the Central Universities (China).

Author contributions

Jiao Xue and Xun Sun designed the research. Jiao Xue, Yining Zhu, Shuting Bai and Chunting He carried out the experiments and performed data analysis. Yao Zhong, Wenfei Chen and Hairui Wang participated part of the experiments. Jiao Xue wrote the manuscript. Xun Sun, Jiao Xue, Yining Zhu, Guangsheng Du and Yuandong Zhang revised the manuscript. All of the authors have read and approved the final manuscript.

Conflicts of interest

The authors declare no conflicts of interest.

Appendix A. Supporting information

Supporting data to this article can be found online at https://doi.org/10.1016/j.apsb.2021.11.020.

References

1. Na IK, Buckland M, Agostini C, Edgar JDM, Friman V, Michallet M, et al. Current clinical practice and challenges in the management of secondary immunodeficiency in hematological malignancies. *Eur J Haematol* 2019;**102**:447–56.
2. Beik J, Abed Z, Ghoreishi FS, Hosseini-Nami S, Mehrzadi S, Shakeri-Zadeh A, et al. Nanotechnology in hyperthermia cancer therapy: from fundamental principles to advanced applications. *J Control Release* 2016;**235**:205–21.
3. Zhu YN, Xue J, Chen WF, Bai ST, Zheng T, He CT, et al. Albumin-biomineralized nanoparticles to synergize phototherapy and immunotherapy against melanoma. *J Control Release* 2020;**322**:300–11.
4. Fidele NB, Zheng YY, Zhao YF, Wu TF, Liu JY, Sun YF, et al. Recurrence of odontogenic keratocysts and possible prognostic factors: review of 455 patients. *Med Oral Patol Oral Cir Bucal* 2019;**24**:e491–501.
5. Liu Y, Crawford BM, Vo-Dinh T. Gold nanoparticles-mediated photothermal therapy and immunotherapy. *Immunotherapy* 2018;**10**:1175–88.
6. Liang X, Ye XY, Wang C, Xing CY, Miao QW, Xie ZJ, et al. Photothermal cancer immunotherapy by erythrocyte membrane-coated black phosphorus formulation. *J Control Release* 2019;**296**:150–61.
7. Ye X, Liang X, Chen Q, Miao QW, Chen XL, Zhang XD, et al. Surgical tumor-derived personalized photothermal vaccine formulation for cancer immunotherapy. *ACS Nano* 2019;**13**:2956–68.
8. Zhang F, Lu GH, Wen XL, Li F, Ji XY, Li QQ, et al. Magnetic nanoparticles coated with polyphenols for spatio-temporally controlled cancer photothermal/immunotherapy. *J Contr Release* 2020;**326**:131–9.
9. Li QQ, Shi ZQ, Zhang F, Zeng WW, Zhu DW, Mei L. Symphony of nanomaterials and immunotherapy based on the cancer–immunity cycle. *Acta Pharm Sin B* 2021. Available from: https://doi.org/10.1016/j.apsb.2021.
10. Chen WF, Qin M, Chen XY, Wang Q, Zhang ZR, Sun X. Combining photothermal therapy and immunotherapy against melanoma by polydopamine-coated Al_2O_3 nanoparticles. *Theranostics* 2018;**8**:2229–41.
11. Dreyer DR, Miller DJ, Freeman BD, Paul DR, Bielawski CW. Elucidating the structure of poly(dopamine). *Langmuir* 2012;**28**:6428–35.
12. Lee H, Dellatore SM, Miller WM, Messersmith PB. Mussel-inspired surface chemistry for multifunctional coatings. *Science* 2007;**318**:426–30.
13. Müller M, Kessler B. Deposition from dopamine solutions at Ge substrates: an *in situ* ATR-FTIR study. *Langmuir* 2011;**27**:12499–505.
14. Chen WF, Wang Y, Qin M, Zhang XD, Zhang ZR, Sun X, et al. Bacteria-driven hypoxia targeting for combined biotherapy and photothermal therapy. *ACS Nano* 2018;**12**:5995–6005.
15. Burzio LA, Waite JH. Cross-linking in adhesive quinoproteins: studies with model decapeptides. *Biochemistry* 2000;**39**:11147–53.
16. Aggarwal P, Hall JB, McLeland CB, Dobrovolskaia MA, McNeil SE. Nanoparticle interaction with plasma proteins as it relates to particle biodistribution, biocompatibility and therapeutic efficacy. *Adv Drug Deliv Rev* 2009;**61**:428–37.
17. Saw WS, Ujihara M, Chong WY, Voon SH, Imae T, Kiew LV, et al. Size-dependent effect of cystine/citric acid-capped confeito-like gold nanoparticles on cellular uptake and photothermal cancer therapy. *Colloids Surf, B* 2018;**161**:365–74.
18. Gratton SE, Ropp PA, Pohlhaus PD, Luft JC, Madden VJ, Napier ME, et al. The effect of particle design on cellular internalization pathways. *Proc Natl Acad Sci U S A* 2008;**105**:11613–8.
19. Kolhar P, Anselmo AC, Gupta V, Pant K, Prabhakarpandian B, Ruoslahti E, et al. Using shape effects to target antibody-coated nanoparticles to lung and brain endothelium. *Proc Natl Acad Sci U S A* 2013;**110**:10753–8.
20. Salatin S, Maleki Dizaj S, Yari Khosroushahi A. Effect of the surface modification, size, and shape on cellular uptake of nanoparticles. *Cell Biol Int* 2015;**39**:881–90.
21. Hühn D, Kantner K, Geidel C, Brandholt S, De Cock I, Soenen SJ, et al. Polymer-coated nanoparticles interacting with proteins and cells: focusing on the sign of the net charge. *ACS Nano* 2013;**7**:3253–63.
22. Mohanty RP, Liu X, Ghosh D. Electrostatic driven transport enhances penetration of positively charged peptide surfaces through tumor extracellular matrix. *Acta Biomater* 2020;**113**:240–51.
23. Yoo HS, Lee JE, Chung H, Kwon IC, Jeong SY. Self-assembled nanoparticles containing hydrophobically modified glycol chitosan for gene delivery. *J Contr Release* 2005;**103**:235–43.
24. Shan W, Zhu X, Liu M, Li L, Zhong JJ, Sun W, et al. Overcoming the diffusion barrier of mucus and absorption barrier of epithelium by self-assembled nanoparticles for oral delivery of insulin. *ACS Nano* 2015;**9**:2345–56.
25. Wang S, Guo H, Li YF, Li XJ. Penetration of nanoparticles across a lipid bilayer: effects of particle stiffness and surface hydrophobicity. *Nanoscale* 2019;**11**:4025–34.
26. Guo P, Liu DX, Subramanyam K, Wang BR, Yang J, Huang J, et al. Nanoparticle elasticity directs tumor uptake. *Nat Commun* 2018;**9**:130.
27. Hou Y, Yu LX, Xie WY, Camacho LC, Zhang M, Chu ZQ, et al. Surface roughness and substrate stiffness synergize to drive cellular mechanoresponse. *Nano Lett* 2020;**20**:748–57.
28. Rowshanravan B, Halliday N, Sansom DM. CTLA-4: a moving target in immunotherapy. *Blood* 2018;**131**:58–67.
29. Boutros C, Tarhini A, Routier E, Lambotte O, Ladurie FL, Carbonnel F, et al. Safety profiles of anti-CTLA-4 and anti-PD-1 antibodies alone and in combination. *Nat Rev Clin Oncol* 2016;**13**:473–86.

30. Hellmann MD, Paz-Ares L, Bernabe Caro R, Zurawski B, Kim SW, Carcereny Costa E, et al. Nivolumab plus ipilimumab in advanced non-small-cell lung cancer. *N Engl J Med* 2019;**381**:2020−31.
31. Gao X, McDermott DF. Ipilimumab in combination with nivolumab for the treatment of renal cell carcinoma. *Expet Opin Biol Ther* 2018; **18**:947−57.
32. Adeegbe DO, Liu Y, Lizotte PH, Kamihara Y, Aref AR, Almonte C, et al. Synergistic immunostimulatory effects and therapeutic benefit of combined histone deacetylase and bromodomain inhibition in non-small cell lung cancer. *Cancer Discov* 2017;**7**:852−67.
33. Zhu H, Bengsch F, Svoronos N, Rutkowski MR, Bitler BG, Allegrezza MJ, et al. BET bromodomain inhibition promotes anti-tumor immunity by suppressing PD-L1 expression. *Cell Rep* 2016; **16**:2829−37.
34. Zhou FQ, Gao J, Xu ZA, Li TL, Gao A, Sun F, et al. Overcoming immune resistance by sequential prodrug nanovesicles for promoting chemoimmunotherapy of cancer. *Nano Today* 2021;**36**: 101025.
35. Sun F, Zhu QR, Li TL, Saeed M, Xu ZA, Zhong F, et al. Regulating glucose metabolism with prodrug nanoparticles for promoting photoimmunotherapy of pancreatic cancer. *Adv Sci (Weinh)* 2021;**8**: 2002746.
36. Hou B, Zhou L, Wang H, Saeed M, Wang DG, Xu ZA, et al. Engineering stimuli-activatable boolean logic prodrug nanoparticles for combination cancer immunotherapy. *Adv Mater* 2020;**32**: e1907210.
37. Adeegbe DO, Liu S, Hattersley MM, Bowden M, Zhou CW, Li S, et al. BET bromodomain inhibition cooperates with PD-1 blockade to facilitate antitumor response in *Kras*-mutant non-small cell lung cancer. *Cancer Immunol Res* 2018;**6**:1234−45.
38. Wang HR, Tang YS, Fang YF, Zhang M, Wang HY, He ZD, et al. Reprogramming tumor immune microenvironment (TIME) and metabolism *via* biomimetic targeting codelivery of Shikonin/JQ1. *Nano Lett* 2019;**19**:2935−44.
39. Kishimoto T, Hagi K, Nitta M, Leucht S, Olfson M, Kane JM, et al. Effectiveness of long-acting injectable *vs* oral antipsychotics in patients with schizophrenia: a meta-analysis of prospective and retrospective cohort studies. *Schizophr Bull* 2018;**44**:603−19.
40. Kurosky SK, Davis KL, Krishnarajah G. Effect of combination vaccines on completion and compliance of childhood vaccinations in the United States. *Hum Vaccines Immunother* 2017;**13**: 2494−502.
41. Ku SH, Ryu J, Hong SK, Lee H, Park CB. General functionalization route for cell adhesion on non-wetting surfaces. *Biomaterials* 2010;**31**: 2535−41.
42. Hong XY, Zhong XF, Du GS, Hou YY, Zhang YT, Zhang ZR, et al. The pore size of mesoporous silica nanoparticles regulates their antigen delivery efficiency. *Sci Adv* 2020;**6**:eaaz4462.
43. Liu YL, Ai KL, Liu JH, Deng M, He YY, Lu LH. Dopamine-melanin colloidal nanospheres: an efficient near-infrared photothermal therapeutic agent for *in vivo* cancer therapy. *Adv Mater* 2013;**25**:1353−9.
44. Chen D, Li LL, Tang FQ, Qi S. Facile and scalable synthesis of tailored silica "nanorattle" structures. *Adv Mater* 2009;**21**: 3804−7.
45. Liu YL, Ai KL, Lu LH. Polydopamine and its derivative materials: synthesis and promising applications in energy, environmental, and biomedical fields. *Chem Rev* 2014;**114**:5057−115.
46. Huber V, Camisaschi C, Berzi A, Ferro S, Lugini L, Triulzi T, et al. Cancer acidity: an ultimate frontier of tumor immune escape and a novel target of immunomodulation. *Semin Cancer Biol* 2017;**43**: 74−89.
47. Major M, Law M. Detection of antibodies to HCV E1E2 by lectin-capture ELISA. *Methods Mol Biol* 2019;**1911**:421−32.
48. Hung BP, Hutton DL, Grayson WL. Mechanical control of tissue-engineered bone. *Stem Cell Res Ther* 2013;**4**:10.
49. Zou WP, Wolchok JD, Chen LP. PD-L1 (B7-H1) and PD-1 pathway blockade for cancer therapy: mechanisms, response biomarkers, and combinations. *Sci Transl Med* 2016;**8**:328rv4.
50. Conner SD, Schmid SL. Regulated portals of entry into the cell. *Nature* 2003;**422**:37−44.
51. Barone A, Hazarika M, Theoret MR, Mishra-Kalyani P, Chen H, He K, et al. FDA approval summary: pembrolizumab for the treatment of patients with unresectable or metastatic melanoma. *Clin Cancer Res* 2017;**23**:5661−5.
52. Beaver JA, Theoret MR, Mushti S, He K, Libeg M, Goldberg K, et al. FDA approval of Nivolumab for the first-line treatment of patients with BRAF(V600) wild-type unresectable or metastatic melanoma. *Clin Cancer Res* 2017;**23**:3479−83.
53. Francis DM, Manspeaker MP, Schudel A, Sestito LF, O'Melia MJ, Kissick HT, et al. Blockade of immune checkpoints in lymph nodes through locoregional delivery augments cancer immunotherapy. *Sci Transl Med* 2020;**12**:eaay3575.
54. Francis DM, Thomas SN. Progress and opportunities for enhancing the delivery and efficacy of checkpoint inhibitors for cancer immunotherapy. *Adv Drug Deliv Rev* 2017;**114**:33−42.
55. Thurber GM, Schmidt MM, Wittrup KD. Antibody tumor penetration: transport opposed by systemic and antigen-mediated clearance. *Adv Drug Deliv Rev* 2008;**60**:1421−34.
56. Sagiv-Barfi I, Czerwinski DK, Levy S, Alam IS, Mayer AT, Gambhir SS, et al. Eradication of spontaneous malignancy by local immunotherapy. *Sci Transl Med* 2018;**10**:eaan4488.
57. Ingram JR, Blomberg OS, Sockolosky JT, Ali L, Schmidt FI, Pishesha N, et al. Localized CD47 blockade enhances immunotherapy for murine melanoma. *Proc Natl Acad Sci U S A* 2017;**114**: 10184−9.